

Porous carbon nanowire array for highly sensitive, biocompatible, reproducible surface-enhanced Raman spectroscopy

Nan Chen^{1,2,†}, Ting-Hui Xiao^{1,†}, Zhenyi Luo¹, Yasutaka Kitahama¹, Kotaro Hiramatsu¹, Tamitake Itoh³, Zhenzhou Cheng^{1,4} & Keisuke Goda^{1,5,6*}

1 Department of Chemistry, The University of Tokyo, Tokyo 113-0033, Japan

2 School of Chemistry and Chemical Engineering, Beijing Institute of Technology, Beijing 100081, P. R. China

3 Health Research Institute, National Institute of Advanced Industrial Science and Technology, Takamatsu 761-0395, Japan

4 Department of Optoelectronic Information Engineering, Tianjin University, Nankai 300011, P. R. China

5 Institute of Technological Sciences, Wuhan University, Wuhan 430072, P. R. China

6 Department of Bioengineering, University of California, Los Angeles, California 90095, USA

*E-mail: goda@chem.s.u-tokyo.ac.jp

Surface-enhanced Raman spectroscopy (SERS) is a powerful tool for vibrational spectroscopy as it provides several orders of magnitude higher sensitivity than inherently weak spontaneous Raman scattering by exciting localized surface plasmon resonance (LSPR) on metal substrates¹⁻⁴. However, SERS is not very reliable, especially for use in life sciences, since it sacrifices reproducibility and biocompatibility due to its strong dependence on “hot spots”⁵⁻⁷ and large photothermal heat generation^{8,9}. Here we report a metal-free (i.e., LSPR-free), topologically tailored nanostructure composed of porous carbon nanowires in an array as a SERS substrate that addresses the decades-old problem. Specifically, it offers not only high signal enhancement due to its strong broadband charge-transfer resonance, but also extraordinarily high reproducibility or substrate-to-substrate, spot-to-spot, sample-to-sample, and time-to-time consistency in SERS spectrum due to the absence of hot spots and high compatibility to biomolecules due to its fluorescence quenching and negligible denaturation capabilities. These excellent properties make SERS suitable for practical use in diverse biomedical applications.

Since its discovery in the 1970s, SERS has gained popularity as an analytical method for its extraordinarily high signal enhancement¹⁰⁻¹². Unfortunately, the benefit of SERS is compromised by its extremely poor reproducibility and biocompatibility due to its dependence on hot spots for high enhancement factors from aggregates of metal nanoparticles^{13,14} or engineered metal nanostructures^{4,6,7} and the generation of large photothermal heat on the metal surface that causes detrimental effects to biomolecules (e.g., heat-induced protein denaturation)^{8,9}. In recent years, non-metallic materials such as silicon and germanium nanostructures¹⁵⁻¹⁸, two-dimensional materials (e.g., graphene, MoS₂, and h-BN)¹⁹⁻²², and semiconducting metal oxides²³⁻²⁴ have been proposed as alternative SERS substrates to circumvent the fundamental problem of traditional SERS. Different from the metal substrates that mainly rely on LSPR, their signal enhancement originates from structural

resonance¹⁶⁻¹⁸ or charge transfer resonance^{22,23} and has been demonstrated with decent enhancement factors of up to five orders of magnitude^{16-18,22,23}. However, the poor reproducibility remains a major challenge while these substrates partly address the biocompatibility issue. This is due to their inherent photocatalytic activity and the toxicity of their substrate material to biomolecules²⁵⁻²⁷.

In this Letter, we take a radically different approach from the metal, semiconducting, and dielectric substrates and demonstrate that a metal-free (i.e., LSPR-free), topologically tailored nanostructure composed of a two-dimensional array of porous carbon nanowires is an effective material as a substrate for highly sensitive, biocompatible, and reproducible SERS (Supplementary Table 1). Specifically, the porous carbon nanowire array (PCNA) substrate provides not only high signal enhancement ($\sim 10^6$) due to its strong broadband charge-transfer resonance for large chemical enhancement (as opposed to electromagnetic enhancement in traditional SERS), but also extraordinarily high reproducibility or substrate-to-substrate, spot-to-spot, sample-to-sample, and time-to-time consistency in SERS spectrum (which is not possible with traditional SERS) due to the absence of hot spots and high compatibility to biomolecules due to its fluorescence quenching and negligible denaturation capabilities. We experimentally demonstrate these excellent properties with various molecules such as rhodamine 6G (R6G), β -lactoglobulin, and glucose. To the best of our knowledge, our PCNA substrates offers the highest reproducibility and biocompatibility to date, holding great promise for reliable SERS in practical use, especially in areas of analytical chemistry, pharmaceutical science, food science, forensic science, and pathology where inconsistent or non-reproducible SERS spectra have been problematic.

The synthesis and material properties of the PCNA are described as follows and shown in Fig. 1a through Fig. 1d. First, a polypyrrole (PPy) nanowire array (PNA) is prepared through a conventional template-assisted electropolymerization method²⁸ with an anodized aluminum oxide (AAO) template (Supplementary Fig. 1). Second, a working electrode is interchanged with a counter electrode. Then, the PNA undergoes an electrical degradation process in a high-temperature dimethyl sulfoxide (DMSO) solution containing sulfur clusters under an oppositely applied voltage to form a large number of nanopores in each PPy nanowire, which transforms into a porous polypyrrole nanowire array (PPNA) and effectively increases the specific surface area (SSA) and roughness. Finally, a carbonization process at an elevated temperature is applied to the PPNA to generate a SERS-active PCNA (Supplementary Figs. 2 and 3). Each porous nanowire of the PCNA has an average diameter of 140 nm and an average length of 15 μm after the carbonization (Fig. 1a), which is in agreement with those of the AAO template. An enlarged scanning electron microscope (SEM) image of the PCNA reveals that numerous holes with an average diameter of about 50 nm are distributed on the PCNA, resulting in fractal nanostructures with a high SSA (Supplementary Figs. 4 and 5). In addition, as shown in Fig. 1b, results from our Raman spectroscopy of the PPNA and PCNA indicate that all the characteristic Raman peaks of the PPNA at 870, 930, 1050, and 1246 cm^{-1} disappeared from the PCNA after the carbonization, as expected. As shown in Fig. 1c, results from our current-voltage (I - V) curve measurements of the PPNA and PCNA indicate that the porous carbon nanomaterial performs as a semiconductor since the carbonization treatment significantly increases its conductivity (Supplementary Figs. 6 and 7). Moreover, results from our energy dispersive X-ray spectroscopy

(EDS) of the PPNA and PCNA indicate that the composition ratio of carbon significantly increased after the carbonization process as shown in Fig. 1d.

To demonstrate the high adsorptivity and reproducibility of the PCNA as a SERS substrate, we performed SERS of R6G (a highly fluorescent rhodamine family dye) on the PCNA substrate. For comparison, we obtained Raman spectra of R6G molecules adsorbed on silicon, PNA, carbon nanowire array (CNA), and PCNA substrates under the same conditions (a 10- μ M deionized water solution of R6G molecules, an integration time of 30 s, continuous-wave laser illumination with 1 mW at 785 nm), as shown in Fig. 2a (Supplementary Fig. 8 and Supplementary Table 2). In comparison to the other substrates, the PCNA exhibits the highest Raman signal intensity, indicating its high adsorptivity (i.e., large surface-to-volume ratio), which originates from its porous nanowire morphology and carbon-based material. Moreover, to evaluate the sensitivity of the PCNA substrate, we obtained SERS spectra of R6G molecules at reduced concentrations on the PCNA substrate (Fig. 2b). It is evident from the figure that the detection limit of the PCNA substrate for R6G molecules is about 10 nM, which is challenging with conventional metal substrates due to the strong fluorescence of R6G molecules that obscure their weak Raman signal. It is important to note that the use of carbon quenched the fluorescent property of R6G molecules, indicating the ability of the PCNA substrate to analyze biomolecules which are mostly fluorescent. Similar SERS measurements were performed on DMSO to verify the high sensitivity of the PCNA substrate (Supplementary Fig. 9). As shown in Fig. 2c, the PCNA substrate shows a monotonically increasing relation between the R6G concentration and signal intensity at 1185, 1309, 1361, 1507, and 1650 cm^{-1} . Furthermore, in order to assess the substrate-to-substrate consistency of the PCNA substrate, we carried out a measurement reproducibility test on 20 different PCNA substrates. As shown in Fig. 2d, the differences in the relative intensities of the Raman peaks at 1185, 1309, 1361, 1507, and 1650 cm^{-1} between all of the substrates are with a standard deviation of 5.7%, indicating the high reliability of the PCNA substrate.

Next, to demonstrate the highly sensitive detection of biomolecules, we conducted SERS of β -lactoglobulin (the major whey protein of cow and sheep's milk) on the PCNA substrate. With an integration time of 300 s and an excitation illumination of 2 mW at 785 nm, we measured a spontaneous Raman spectrum of a β -lactoglobulin powder with a mass fraction (Mf) of 100% on a bare silicon substrate as ground truth (Fig. 3a, Supplementary Fig. 8, and Supplementary Table 2). Then, by decreasing the integration time to 1 s and the Mf to 0.4%, we obtained the Raman spectrum of β -lactoglobulin molecules with a similar Raman signal intensity on the PCNA substrate. As the ratio of the number of molecules of a β -lactoglobulin solution to that of the β -lactoglobulin powder in the probed volume is approximately equal to their Mf ratio (Supplementary Table 3), we used the Mf ratio to calculate the SERS enhancement, based on which the enhancement factor was found to be $(300 \text{ s} / 1 \text{ s}) \times (100\% / 0.4\%) \times (60000 / 2000) = \sim 10^6$ for β -lactoglobulin. It is important to note that the characteristic Raman peaks of β -lactoglobulin molecules on the PCNA substrate are well distinguishable and consistent with those of the ground truth, indicating the high biocompatibility of the PCNA substrate. For comparison, we also acquired the Raman spectra of β -lactoglobulin molecules on a silicon substrate and a commercial metal SERS substrate (silver-gold hybrid substrate, SERSitive Co.) under the same conditions, as shown in Fig. 3a. On the silicon

substrate, no characteristic Raman peaks were visible due to the absence of the SERS enhancement whereas on the metal substrate, the Raman spectrum was enhanced, but with 10 times weaker than on the PCNA substrate. Also, the characteristic Raman peaks of β -lactoglobulin molecules on the metal substrate do not agree with those of the ground truth obtained from the silicon substrate (Fig. 3a). Finally, to assess the spot-to-spot consistency of the PCNA substrate in Raman signal intensity, we conducted SERS mapping of β -lactoglobulin on the PCNA substrate at two characteristic Raman peaks of the molecule (999 cm^{-1} and 1447 cm^{-1}) on both large and small scales (Fig. 3b). As shown in Fig. 3c, the PCNA substrate has a coefficient of variation (CV) of less than 7.8% on average, which is much smaller than that of the conventional metal substrate (Supplementary Fig. 10). These results firmly demonstrated that the PCNA substrate would be an excellent platform for reliable trace detection of proteins which are typically vulnerable to heat (i.e., prone to denaturation) and are difficult to probe on metal substrates.

Finally, to demonstrate the sample-to-sample consistency of the PCNA substrate in enhancement factor, we conducted SERS of glucose (a well-known biomarker for detecting diabetes²⁹, which has been a challenging molecule for undistorted SERS detection. Fig. 3d shows the Raman spectra of a deionized water solution of glucose molecules on silicon and PCNA substrates under light excitation at 785 nm, with the former used as a ground truth (Supplementary Fig. 8 and Supplementary Table 2). On the PCNA substrate, all the characteristic Raman peaks of glucose molecules were clearly identified and distinguished even at a low Mf of 0.1%, corresponding to a concentration of 5.6 mM (which agrees with the typical glucose concentration of 3-7 mM in the blood of healthy people as opposed to 10-20 mM in the blood of diabetes patients³⁰. Similar to that of β -lactoglobulin, we used the Mf ratio of glucose to calculate the SERS enhancement (Supplementary Table 3), based on which the comparison of the Raman spectra on the silicon and PCNA substrates yields an enhancement factor of $(300\text{ s} / 1\text{ s}) \times (100\% / 0.1\%) \times (1600 / 500) = \sim 10^6$, which is consistent with the enhancement factor of the β -lactoglobulin measurements above. Importantly, even with this high signal enhancement, the locations of the measured characteristic Raman peaks of glucose molecules agree well with those of the ground truth (while each Raman peak has a different chemical enhancement), which is attributed to the high biocompatibility and photothermal stability of the PCNA substrate. Furthermore, to show the time-to-time consistency of the PCNA substrate, we performed SERS measurements of glucose under the same conditions every hour. As shown in Fig. 3e, the Raman spectrum of glucose molecules is temporally stable with negligible denaturation, further demonstrating the high reliability of the PCNA substrate (Supplementary Fig. 11).

The SERS signal enhancement of the PCNA is mainly attributed to the chemical mechanism (CM) for the following reasons. First, carbon provides a high charge-transfer efficiency¹⁴, which greatly increases its Raman-scattering cross-section. An energy level diagram that illustrates the charge transfer of the PCNA-molecule system is depicted in Fig. 4a. The energy of the excitation light (at a wavelength of 785 nm, corresponding to 1.58 eV) in the above experiments is far from the molecular resonance energy, that is, the energy gap between the highest occupied molecular orbital (HOMO) and lowest unoccupied molecular orbital (LUMO). Therefore, the molecular resonance cannot be directly used to enhance the Raman signal. However, as shown in Fig. 4a, the

HOMO and LUMO are bridged by the assistance of the energy bands of the PCNA substrate, enabling two possible resonant charge-transfer pathways. One is from the conduction band of the PCNA to the LUMO of the molecules while the other is from the HOMO to the conduction band, which significantly enhances the Raman signal. Therefore, the SERS enhancement factors of both the PCNA and CNA substrates are much higher than that of the PNA as evidenced by Fig. 2a. Second, H, N, and S atoms in the hydroxyl group that are not completely removed after the carbonization (Fig. 1d) further promote the charge transfer between the substrate and molecules¹⁴, contributing to the SERS enhancement. Finally, the reason for the higher enhancement factor of the PCNA substrate than the CNA substrate (Fig. 2a) is that its porous morphology leads to the higher electric field magnitude as shown in Fig. 4b. However, this electric field increase is too low to account for the extraordinarily high enhancement factor of the PCNA substrate, thereby excluding the electromagnetic mechanism (EM) as the dominant enhancement factor.

To verify this theory experimentally, we performed the following experiments. First, we measured the absorption spectrum of the PCNA substrate with β -lactoglobulin on it as shown in Fig. 4c. The broadband absorption spectrum covers both the excitation wavelength (785 nm) and Stokes Raman wavelengths, indicating an electronic band essential for the efficient charge-transfer resonance. The broad bandwidth of the absorption spectrum also excludes the EM which normally possesses a narrow bandwidth due to its structural resonance. Second, we measured the Raman spectrum of the same molecule up to the high Raman shift region (up to 3200 cm^{-1}) which covers overtones and combination bands of the molecule as shown in Fig. 4d. No peaks of overtones and combination bands were observed in the region. As overtones and combination bands are nonlinear optical effects whose magnitudes are determined by the electric field magnitude and normally evident in EM-based SERS, the absence of their peaks in this region excludes the EM, further verifying the CM as the dominant effect of the Raman enhancement. Third, we measured the Raman spectrum of β -lactoglobulin at different excitation wavelengths (785 nm and 532 nm). As shown in Fig. 4e, enhancement factors of $\sim 10^6$ and $\sim 10^5$ at an excitation wavelength of 785 nm and 532 nm, respectively, were observed, verifying the broadband CM enhancement of the PCNA substrate.

Data availability

All data supporting the findings of this study are included in the article and its Supplementary Information, and are also available from the authors upon reasonable request.

Code availability

All codes used for analysis of this study are available from the authors upon reasonable request.

References

1. Laing, S. *et al.* Surface-enhanced Raman spectroscopy for in vivo biosensing. *Nat. Rev. Chem.* **1**, 0060 (2017).

2. Li, J. F. *et al.* Shell-isolated nanoparticle-enhanced Raman spectroscopy. *Nature* **464**, 392-395 (2010).
3. Aikens, C. M. *et al.* The effect of field gradient on SERS. *Nat. Photon.* **7**, 508-510 (2013).
4. Wu, D. Y. *et al.* Electrochemical surface-enhanced Raman spectroscopy of nanostructures. *Chem. Soc. Rev.* **37**, 1025–1041 (2008).
5. Willets, K. A. Super-resolution imaging of SERS hot spots. *Chem. Soc. Rev.* **43**, 3854–3864 (2014).
6. Shi, X. *et al.* Enhanced water splitting under modal strong coupling conditions. *Nat. Nanotechnol.* **13**, 953–958 (2018).
7. Ding, S. Y. *et al.* Nanostructure-based plasmon-enhanced Raman spectroscopy for surface analysis of materials. *Nat. Rev. Mater.* **1**, 16021 (2016).
8. Caldarola, M. *et al.* Non-plasmonic nanoantennas for surface enhanced spectroscopies with ultra-low heat conversion. *Nat. Commun.* **6**, 7915 (2015).
9. Cong, S. *et al.* Noble metal-comparable SERS enhancement from semiconducting metal oxides by making oxygen vacancies. *Nat. Commun.* **6**, 7800 (2015).
10. Lim, D. K. *et al.* Highly uniform and reproducible surface-enhanced Raman scattering from DNA-tailorable nanoparticles with 1-nm interior gap. *Nat. Nanotechnol.* **6**, 452-460 (2011).
11. Lombardi, J. R. *et al.* A unified view of surface-enhanced Raman scattering. *Acc. Chem. Res.* **42**, 734–742 (2009).
12. Yamamoto, Y. S. *et al.* Why and how do the shapes of surface-enhanced Raman scattering spectra change? Recent progress from mechanistic studies. *J. Raman. Spectrosc.* **47**, 78-88 (2016).
13. Brolo, A. G. Plasmonics for future biosensors. *Nat. Photon.* **6**, 709–713 (2012).
14. Itoh, T. *et al.* Plasmon-enhanced spectroscopy of absorption and spontaneous emissions explained using cavity quantum optics. *Chem. Soc. Rev.* **46**, 3904-3921 (2017).
15. Evlyukhin, A. B. *et al.* Demonstration of magnetic dipole resonances of dielectric nanospheres in the visible region. *Nano Lett.* **12**, 3749-3755 (2012).
16. Wells, S. M. *et al.* Silicon nanopillars for field-enhanced surface spectroscopy. *ACS Nano* **6**, 2948–2959 (2012).
17. He, Y. *et al.* Silicon nanowires-based highly-efficient SERS-active platform for ultrasensitive DNA detection. *Nano Today* **6**, 122-130 (2011).
18. Dmitriev, P. A. *et al.* Resonant Raman scattering from silicon nanoparticles enhanced by magnetic response. *Nanoscale* **8**, 9721-9726 (2016).
19. Feng, S. M. *et al.* Ultrasensitive molecular sensor using n-doped graphene through enhanced Raman scattering. *Sci. Adv.* **2**, e1600322 (2016).
20. Ling, X. *et al.* Can graphene be used as a substrate for Raman enhancement? *Nano Lett.* **10**, 553-561 (2010).
21. Ling, X. *et al.* Raman enhancement effect on two-dimensional layered materials: Graphene, h-BN and MoS₂. *Nano Lett.* **14**, 3033-3040 (2014).
22. Park, W. H. *et al.* Out-of-plane directional charge transfer-assisted chemical enhancement in the surface-

- enhanced Raman spectroscopy of a graphene monolayer. *J. Phys. Chem. C* **120**, 24354–24359 (2016).
23. Zheng, Z. H. *et al.* Semiconductor SERS enhancement enabled by oxygen incorporation. *Nat. Commun.* **8**, 1993 (2017).
 24. Musumeci, A. *et al.* SERS of semiconducting nanoparticles (TiO₂ hybrid composites). *J. Am. Chem. Soc.* **131**, 6040–6041 (2009).
 25. Limo, M. J. *et al.* Interactions between metal oxides and biomolecules: from fundamental understanding to applications. *Chem. Rev.* **118**, 11118–11193 (2018).
 26. Djuricic, A. B. *et al.* Toxicity of metal oxide nanoparticles: mechanisms, characterization, and avoiding experimental artefacts. *Small* **11**, 26–44 (2015).
 27. Da Via, L. *et al.* Visible light selective photocatalytic conversion of glucose by TiO₂. *Appl. Catal. B-Environ.* **202**, 281–288 (2017).
 28. Chen, N. *et al.* Electronic logic gates from three-segment nanowires featuring two p-n heterojunctions. *NPG Asia Mater.* **5**, e59 (2013).
 29. Shafer-Peltier, K. E. *et al.* Toward a glucose biosensor based on surface-enhanced Raman scattering. *J. Am. Chem. Soc.* **125**, 588–593 (2003).
 30. Wang, J. Electrochemical glucose biosensors. *Chem. Rev.* **108**, 814–825 (2008).

Acknowledgements This research was supported by JSPS Core-to-Core Program, JSPS KAKENHI (JP18K13798), White Rock Foundation, University of Tokyo GAP Fund, National Natural Science Foundation of China (21671020), and Beijing Natural Science Foundation (2172049).

Author Contributions N. C. and T. H. X. are co-first authors and contributed equally to this work. N. C. and T. H. X. conducted the experiments and theoretical calculations. N. C., T. H. X., Y. K., K. H., Z. C. and K. G. interpreted the data. Z. C. led the work in the lab. K. G. supervised the research team. N. C., T. H. X., Z. C. and K. G. wrote the manuscript. All authors discussed the results and participated in revising the manuscript.

Author Information Reprints and permissions information is available at www.nature.com/reprints. The authors declare no competing financial interests. Correspondence should be addressed to K. G. (goda@chem.s.u-tokyo.ac.jp).

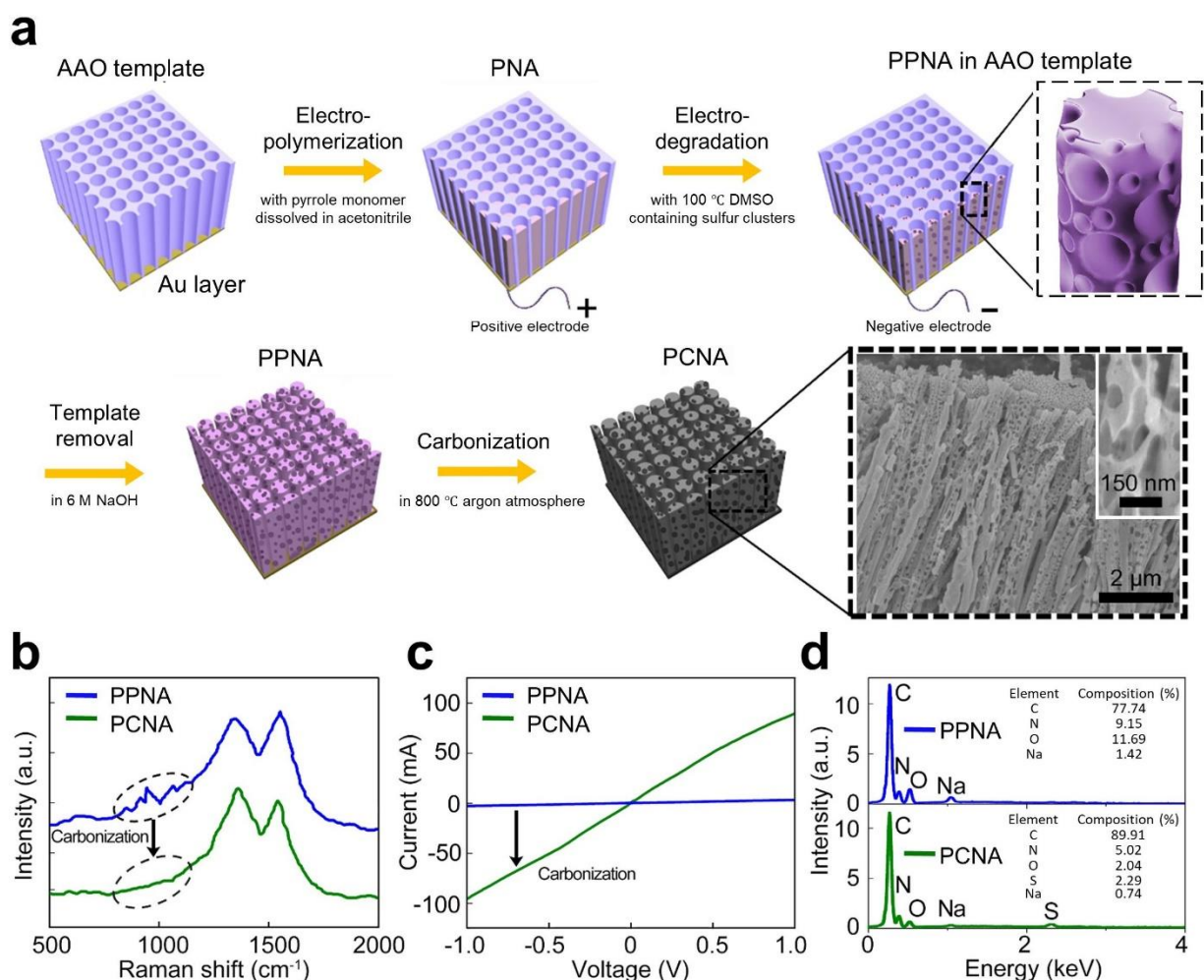


Fig. 1 | Synthesis and characterization of the porous carbon nanowire array (PCNA). **a**, Steps for synthesizing the PCNA. The bottom right inset shows an SEM image of the PCNA and an enlarged SEM image of a single porous carbon nanowire. **b**, Raman spectra of the PPNA and PCNA. After the carbonization process, all the characteristic Raman peaks of the PNA at 870, 930, 1050, and 1246 cm^{-1} disappeared as evident in the PCNA spectrum. **c**, I - V curve measurements of the PPNA and PCNA. In the measurements, the length and contact area of the porous PPy nanowires and porous carbon nanowires are about 15 μm and 0.5 mm^2 , respectively. The conductivity of the substrate was significantly increased after the carbonization process, indicating the semiconducting property of the PCNA. **d**, EDS spectra of the PPNA and PCNA. The composition ratio of carbon was significantly increased after the carbonization process.

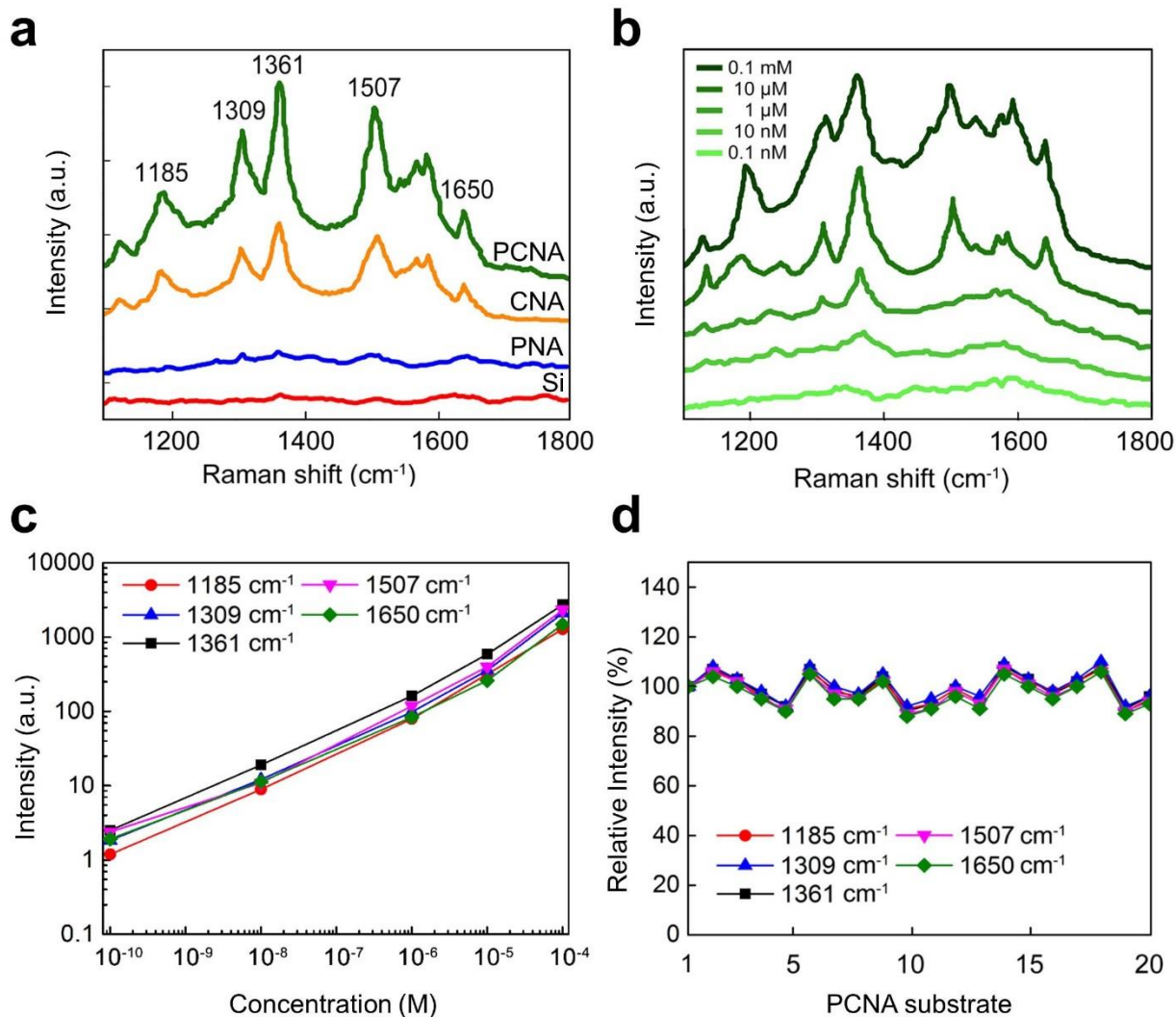


Fig. 2 | SERS of R6G on the PCNA substrate. **a**, Measured Raman spectra of R6G molecules at a concentration of 10 μM on the silicon (red), PNA (blue), CNA (orange), and PCNA (green) substrates for an integration time of 30 s with an excitation power of 1 mW at 785 nm after cleaning the substrates. **b**, Measured Raman spectra of R6G molecules at different concentrations adsorbed on the PCNA substrate for an integration time of 30 s with an excitation power of 1 mW at 785 nm. **c**, Intensities of the Raman peaks at different concentrations at 1185, 1309, 1361, 1507, and 1650 cm^{-1} . The detection limit of the PCNA substrate for R6G molecules is about 10 nM. **d**, SERS reproducibility measurements of R6G molecules on different PCNA substrates. The differences in the relative intensities of the Raman peaks at 1185, 1309, 1361, 1507, and 1650 cm^{-1} between 20 different substrates are within a standard deviation of 5.7%.

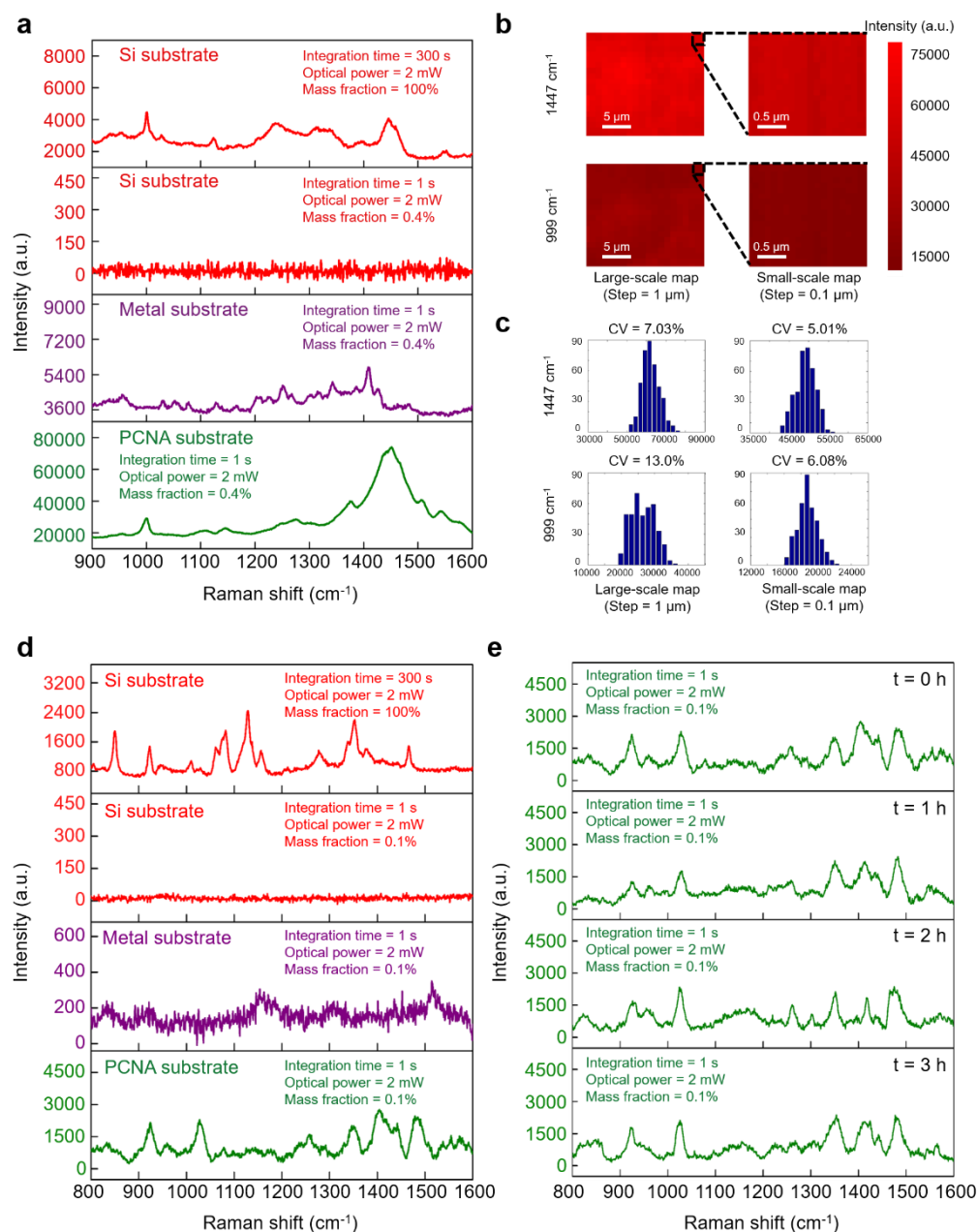


Fig. 3 | SERS of biomolecules (β -lactoglobulin and glucose) on the PCNA substrate. a, Measured Raman spectra of β -lactoglobulin molecules on the silicon, PCNA, and commercial metal substrates. The Raman signal intensity of β -lactoglobulin molecules on the PCNA substrate is 10 times higher than on the metal substrate. **b**, SERS maps of β -lactoglobulin on the PCNA substrate, showing high surface homogeneity in enhancement factor at two characteristic Raman shifts of the molecule on both large and small scales with a step size of 1 μm and 0.1 μm , respectively. **c**, Histograms of the enhancement factors on the large and small scales. **d**, Measured Raman spectra of glucose molecules on the silicon and PCNA substrates. **e**, Time-to-time consistency of the PCNA substrate in the Raman spectrum of glucose. Small hour-to-hour fluctuations in the Raman spectrum indicate high reproducibility and biocompatibility.

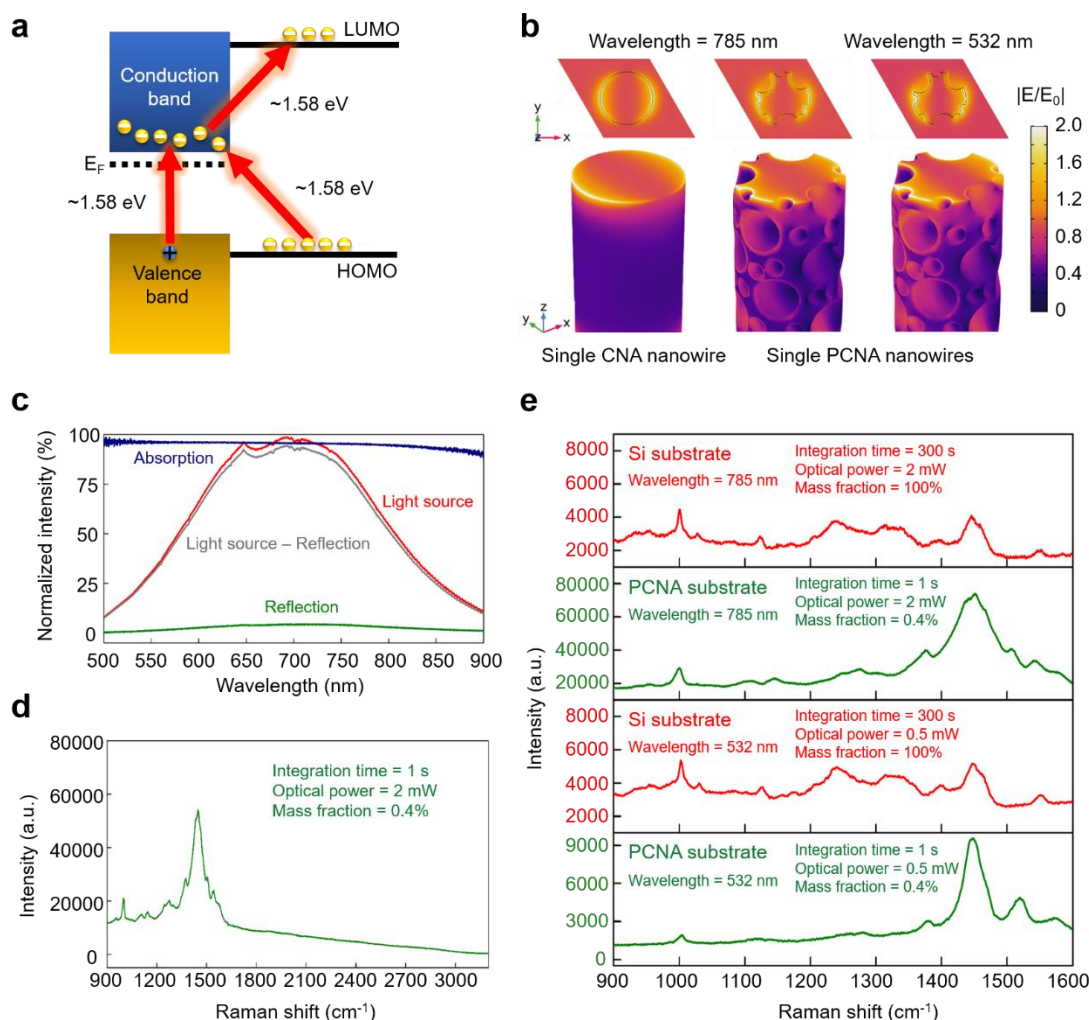


Fig. 4 | Theory and experimental verification of the CM as the dominant effect on the PCNA substrate. a, Energy level diagram of the PCNA-molecule system to explain the CM. The HOMO and LUMO of the molecule are bridged by the assistance of the energy bands of the PCNA substrate, enabling two possible resonant charge-transfer pathways. One is from the conduction band of the PCNA to the LUMO of the molecule while the other is from the HOMO to the conduction band. **b,** Comparison in electric field magnitude distribution between the single CNA nanowire and the single PCNA nanowire to explain the small contribution of the EM. The largest electric field enhancement localized at the lateral edges of each PCNA nanowire is about 2, which corresponds to a small enhancement factor of ~ 16 . Compared with the CNA nanowire without the nanopores, the PCNA nanowire has a larger electric field magnitude due to the sharp edges of its porous structure. Due to the absence of strong structural resonance, the difference between the electric field magnitude distributions at the excitation wavelengths of 532 nm and 785 nm is very small. **c,** Absorption and reflection spectra of the PCNA substrate. **d,** Raman spectrum of β -lactoglobulin up to the high Raman shift region, showing no appreciable peaks of overtones and combination bands. **e,** Raman spectra of β -lactoglobulin at different excitation wavelengths of 532 nm and 785 nm.

Supplementary Information

Porous carbon nanowire array for highly sensitive, biocompatible, reproducible surface-enhanced Raman spectroscopy

Nan Chen^{1,2,†}, Ting-Hui Xiao^{1,†}, Zhenyi Luo¹, Yasutaka Kitahama¹, Kotaro Hiramatsu¹, Tamitake Itoh³, Zhenzhou Cheng^{1,4} & Keisuke Goda^{1,5,6*}

7 *Department of Chemistry, The University of Tokyo, Tokyo 113-0033, Japan*

8 *School of Chemistry and Chemical Engineering, Beijing Institute of Technology, Beijing 100081, P. R. China*

9 *Health Research Institute, National Institute of Advanced Industrial Science and Technology, Takamatsu 761-0395, Japan*

10 *Department of Optoelectronic Information Engineering, Tianjin University, Nankai 300011, P. R. China*

11 *Institute of Technological Sciences, Wuhan University, Wuhan 430072, P. R. China*

12 *Department of Bioengineering, University of California, Los Angeles, California 90095, USA*

*E-mail: goda@chem.s.u-tokyo.ac.jp

Experimental materials

PPy was purchased from Aladdin Bio-Chem Technology Co. Ltd., China. AAO templates with a thickness of 60 μm , a diameter of 13 mm, and an interior porous diameter of 100 nm were purchased from Whatman Co. Ltd., USA. An SEM image of the AAO with a porosity of 50-60% is shown in Supplementary Fig. 1. All the chemicals in this study were purchased from Sigma-Aldrich Co. Inc., China, and used without modification. The commercial metal substrates (the Ag-Au nanoparticle hybrid substrates) were produced by SERSitive Co..

Growth of the PCNA

A conductive layer was obtained by sputtering a 1- μm -thick Au layer on one side of the AAO template before the electropolymerization process. A home-made three-electrode test system, which is composed of an AAO template as the working electrode, a silver/silver chloride electrode as the reference electrode, and a platinum (Pt) foil as the counter electrode, was used to deposit the PNA into the AAO template. During the deposition process, we used a cyclic voltammetry (CV) method at a scan rate of 500 mV/s in a chromatographically pure acetonitrile solution containing 0.1 M LiClO_4 and 0.1 M pyrrole. The electrochemical deposition was performed in a home-made electrochemical cell at room temperature. The electric potential range of the CV method was controlled within 0-1.0 V. After the electrodeposition process, the sample was eluted in deionized water several times. Then, the PNA was treated by the electro-degradation process by using a 100 °C dimethyl sulfoxide (DMSO) solution with suspended sulfur clusters. Nanopores in the PNA were formed by using the CV method at a scan rate of 200 mV/s. Finally, the PPNA was annealed at a temperature of 800 °C for 2 h under an argon atmosphere at a heating rate of 10 °C/min to obtain a PCNA substrate.

Fabrication of the PCNA substrate

The Au layer on the bottom side of the AAO template was first removed by using a mechanical polishing method. Then, the sample was immersed in aqua regia to remove the remaining Au before transferring the PCNA to a bare Si wafer. After that, the AAO template on the Si wafer was removed by using an aqueous NaOH solution with a concentration of 6 M. Since the bottom of the PCNA became interconnected by PPy during the electropolymerization process, the PCNA remained intact after the removal of the Au and AAO template. After being washed in deionized water, the PCNA substrate on the Si wafer was finally obtained. Several PCNA substrates were prepared by using the same recipe. All the PCNA substrates were kept in a sealed and dry environment before characterizations and SERS measurements. Supplementary Fig. 3 shows a black PCNA substrate placed on a white poly tetrafluoroethylene (PTFE) plate.

Methods for characterizing PPNA and PCNA substrates

The morphology and structure of samples (substrates) were characterized by using an SEM (JEOL JSM-7600F) at an accelerating voltage of 5 kV. An energy dispersive X-ray (EDX) detector equipped with the SEM was used to characterize the surface morphology and element composition of the sample at an accelerating voltage of 15 kV. The current-voltage (*I-V*) characteristics of the PPNA and PCNA substrates were recorded with a Keithley 4200 at room temperature in the air, as shown in Supplementary Fig. 6. The specific surface areas (SSAs) were measured by using a nitrogen adsorption-desorption isotherm method at a temperature of 77 K (NOVA 2200e). The Raman spectra of the PPNA and PCNA substrates were obtained by using a RM 2000 microscopic confocal Raman spectrometer (Renishaw PLC, England) excited by a 514-nm-wavelength continuous-wave laser.

SEM imaging of PNA, CNA, and PCNA substrates

SEM images of the PNA, CNA, and PCNA substrates, taken from a JSM-7600F FESEM microscope, were compared in Supplementary Fig. 4a and Supplementary Fig. 4b. These figures clearly show that the electrolysis and carbonization processes had little influence on the surface flatness of the nanowires, respectively. Moreover, the PCNA maintained the original one-dimensional morphology and possess an average diameter of 140 nm after the carbonization process, as shown in Supplementary Fig. 4c.

Thermogravimetric analysis of the PNA

Thermogravimetric analysis (TGA) of the PNA was conducted by using a thermobalance (TGA 2050). In the analysis, the PNA was placed in an Argon atmosphere where the temperature was increased from 20 °C to 800 °C at a rate of 10 °C/min. We found that the PNA began to lose its composition ratio quickly and became carbonized at a temperature of 500 °C, as shown in Supplementary Fig. 2. Therefore, in order to carbonize the PNA sufficiently, we chose 800 °C.

Nitrogen adsorption-desorption isotherm measurements of the PNA and PCNA substrates

The SSAs were determined by conducting nitrogen adsorption-desorption isotherm measurements at a temperature of 77 K (NOVA 2200e). As shown in Supplementary Fig. 5a, the hysteresis loop of the PCNA substrate is larger than that of the PNA at low pressure, indicating an increased number of pores. The Brunauer-Emmett-Teller (BET) SSAs of the PCNA was calculated to be 547.13 m²/g, which is higher than that of the PNA (363.63 m²/g), due to the presence of more nanoholes in the PCNA. Moreover, a large number of pores on the nanowires further increased the surface roughness of the PCNA substrate, as shown in Supplementary Fig. 5b, which contributed to higher enhancement in SERS.

X-ray diffraction measurements of the PCNA

X-ray diffraction (XRD) analysis was performed on the PCNA with a D8 Advance X-ray diffractometer with CuK α radiation ($\lambda = 1.5418 \text{ \AA}$) in the range of 5-80° (2 θ) with a scanning step of 0.05° at a temperature of 25 °C. As shown in Supplementary Fig. 7, the PCNA has two diffraction peaks at 26° and 44°, which correspond to the characteristic peaks of graphite, specifically the (002) and (100) crystal planes of the graphite structure¹. The results showed that the PPNA was successfully carbonized at a temperature of 800 °C to produce partially graphitized carbon.

Raman spectroscopy of DMSO on the silicon and PCNA substrates

To demonstrate trace-amount detection of molecules on the PCNA substrate, we conducted SERS of DMSO, a well-known polar aprotic solvent that dissolves both polar and nonpolar compounds and is miscible in a wide range of organic solvents as well as water. Supplementary Fig. 9 shows that the Raman spectra of DMSO solutions on the silicon and PCNA substrates under light excitation at 785 nm. The Raman spectrum of the DMSO solution with a mass fraction of 100% on the silicon substrate was first measured as a ground truth. On the PCNA substrate, all the characteristic Raman peaks of the DMSO solution were identified and distinguished even at a mass fraction of 5.5 $\times 10^{-8}\%$, corresponding to an enhancement factor of $\sim 10^7$. At a further reduced mass fraction of 5.5 $\times 10^{-9}\%$, no characteristic Raman peaks of the molecules were visible. More importantly, even with such a high signal enhancement, all the measured characteristic Raman peaks of the DMSO solutions agree well with those of the ground truth. No distortion or undesirable shift of the Raman peaks was identified in the measured SERS spectra at the different mass fractions, which is attributed to the excellent sensitivity, biocompatibility, and photothermal stability of the PCNA substrate.

Raman peak assignments of R6G, β -lactoglobulin, glucose, and DMSO

Our Raman peak assignments of R6G, β -lactoglobulin, and glucose are shown in Supplementary Fig. 8a through Supplementary Fig. 8d. For R6G, Supplementary Fig. 8a shows its Raman spectrum on the PCNA substrate after a 30-s incubation in a 10- μ M R6G solution. A detailed assignment of the R6G spectral features has been reported previously², which is highly consistent with our results. In the spectral region between 1000 and 1700 cm⁻¹, a

strong band is evident due to the stretching mode of the carbon skeleton. The stretching modes of the carbon skeleton give rise to the strongest R–R band. Moreover, the C–C stretching modes of R6G result in strong bands at 1185, 1309, 1361, 1507, 1575 and 1650 cm^{-1} in the spectrum. For β -lactoglobulin, its Raman spectra in the spectral range of 900-1600 cm^{-1} with a mass fraction of 0.4% on the silicon and PCNA substrates are shown in Supplementary Fig. 8b. The Raman peak at 1001 cm^{-1} is due to the C–C ring stretching vibrations of phenylalanine (Phe), which is usually separated from other bands and its intensity is not affected by protein conformational changes. The Raman peak at 1245 cm^{-1} is the amide III mode region, which is mainly produced by C–N stretching and N–H in-plane bending vibrations of peptide bonds. The bending and wagging modes of C–H of β -lactoglobulin appear at 1376 and 1454 cm^{-1} . The Raman peak at 1547 cm^{-1} can be assigned to the changes in disulfide conformation as well as in microenvironment around amino acid residues^{3,4}. For glucose, its Raman spectra in the spectral range of 800-1600 cm^{-1} with a mass fraction of 0.1% on the silicon and PCNA substrates are shown in Supplementary Fig. 8c. The Raman peak at 836 cm^{-1} can be assigned to the stretching mode of C–C. The Raman peak at 924 cm^{-1} can be assigned to the bending mode of C–H. The Raman peak at 1028 cm^{-1} can be assigned to the stretching mode of C–O. The Raman peak at 1255 cm^{-1} can be assigned to the twisting mode of CH_2 , while the Raman peaks at 1350 cm^{-1} can be assigned to the wagging mode of CH_2 . The Raman peak at 1403 and 1480 cm^{-1} can be assigned to the bending mode of CH_2 ⁵. For DMSO, the Raman spectra in the spectral range of 500-1500 cm^{-1} with a mass fraction of $5.5 \times 10^{-8}\%$ on the silicon and PCNA substrates are shown in Supplementary Fig. 8d. The C–S stretching mode results in the Raman peaks at 681 and 718 cm^{-1} , while the bending mode of C–H appears at 949 cm^{-1} . The Raman peaks at 1010 cm^{-1} can be assigned to the stretching mode of S=O. The Raman peak at 1311 cm^{-1} can be assigned to the C–H symmetric deformation. Moreover, we attribute the Raman peak at 1419 cm^{-1} to the CH_3 degenerate deformation⁶⁻⁸. The peak assignments of observed Raman shifts of R6G, β -lactoglobulin, glucose, and DMSO are summarized in Supplementary Table 2.

Calculation of the Raman peak intensities of R6G

A baseline correction method was chosen to minimize the effect of fluorescence on the Raman spectrum. In addition, we used a 785-nm-wavelength laser as an excitation light to minimize the fluorescence of R6G. We measured the relative height of the peak intensity to the baseline. The differences in the relative intensities of the Raman peaks at 1185, 1309, 1361, 1507, and 1650 cm^{-1} between all the substrates are with a standard deviation (*SD*) as follows:

$$SD = \sqrt{\frac{1}{N-1} \sum_{i=1}^N (x_i - \bar{x})^2}, \quad (1)$$

where x_i is the relative intensity of each Raman peak, \bar{x} is the average peak intensity of 20 samples at a certain Raman shift. After calculations, we found that the *SD* of the peak intensity at 1361 cm^{-1} (*SD*₁₃₆₁) is 5.647, *SD*₁₁₈₅ is 5.537, *SD*₁₃₀₉ is 5.593, *SD*₁₅₀₇ is 5.540, *SD*₁₆₅₀ is 5.559, respectively. The *SD* of all the peak intensities is 5.686.

Reproducibility testing of the metal substrate in space

To quantitatively compare the metal and PCNA substrates in terms of reproducibility in space, we performed a similar spot-to-spot consistency assessment of a commercial metal substrate. Specifically, we conducted SERS mapping of the metal substrate at two characteristic Raman peaks of β -lactoglobulin (955 cm^{-1} and 1409 cm^{-1}) on both large and small scales, as shown in Supplementary Fig. 10a. The figure shows that there is a significant level of surface inhomogeneity in the enhancement factor, including the existence of position-dependent hot spots. As shown in Supplementary Fig. 10b, the Raman signal intensities measured on the metal substrate has a CV value of more than 25.3% on average, which is much larger than that of the PCNA substrate.

Reproducibility testing of the metal substrate in time

To quantitatively compare the metal and PCNA substrates in terms of reproducibility in time, we performed a time-to-time consistency assessment of the commercial metal substrate. The experimental conditions for this control experiment are identical to those for the PCNA substrate. As shown in Supplementary Fig. 11, several weak Raman peaks of glucose on the commercial metal substrate appeared at $t = 0\text{ h}$. However, no Raman peaks of the glucose molecules on the commercial metal substrate appeared at $t = 1\text{ h}$, 2 h , and 3 h . The results indicate that the metal substrate has a poor time-to-time consistency for SERS measurements.

Estimation of the numbers of molecules of the measured samples in the probed volume

Below we estimate the number of molecules of the measured samples in the probed volume and summarize them in Supplementary Table 3. In our SERS experiments, we used a 50x objective lens with a numerical aperture (NA) of 0.42 to focus the 785-nm incident light onto the samples. Assuming the Airy disc, the probed volume can be approximately calculated by $(0.61\lambda/NA)^3$, where λ is the wavelength of the incident light. From our experimental values, the probed volume is found to be $1.5\text{ }\mu\text{m}^3$.

In the SERS measurement of β -lactoglobulin, we used both β -lactoglobulin powder and solution as the samples. The density of the β -lactoglobulin powder is 1.25 g/cm^3 while its molar mass is $\sim 18,400\text{ g/mol}$ ⁹. Thus, its molar concentration is found to be $(1.25\text{ g/cm}^3) / (18,400\text{ g/mol}) = 0.068\text{ M}$. The total number of molecules of the β -lactoglobulin powder in the probed volume is found to be $0.068\text{ M} \times 1.5\text{ }\mu\text{m}^3 = 1.0 \times 10^{-16}\text{ mol}$. As the density of the β -lactoglobulin solution with a Mf of 0.4% is between 1 g/cm^3 and 1.25 g/cm^3 , which is approximately identical to that of the β -lactoglobulin powder, the ratio of the number of molecules of the β -lactoglobulin solution to that of the β -lactoglobulin powder in the probed volume is approximately equal to their Mf ratio. The total number of molecules of the β -lactoglobulin solution in the probed volume is found to be $1.0 \times 10^{-16} \times 0.4\% / 100\% = 4.0 \times 10^{-19}\text{ mol}$. Therefore, the Mf ratio approximately equals the ratio of the numbers of molecules under enhanced and unenhanced conditions, which is used to calculate the SERS enhancement factor of β -lactoglobulin.

Similarly, in the SERS measurement of glucose, the density and molar mass of the glucose powder are given by 1.56 g/cm^3 and 180 g/mol , respectively. Thus, its molar concentration is found to be 8.7 M . The total number

of molecules of the glucose powder in the probed volume is found to be $8.7 \text{ M} \times 1.5 \text{ } \mu\text{m}^3 = 1.3 \times 10^{-14} \text{ mol}$. As the density of the glucose solution with a Mf of 0.1% is between 1 g/cm^3 and 1.56 g/cm^3 , which is approximately identical to that of the glucose powder, the ratio of the number of molecules of the glucose solution to that of glucose powder in the probed volume is approximately equal to their Mf ratio. The total number of molecules of the glucose solution in the probed volume is found to be $1.3 \times 10^{-14} \times 0.1\% / 100\% = 1.3 \times 10^{-17} \text{ mol}$. Therefore, the Mf ratio that approximately equals the ratio of the numbers of molecules under enhanced and unenhanced conditions is used to calculate the SERS enhancement factor of glucose.

Finally, in the SERS measurement of DMSO, the density and molar mass of pure DMSO are 1.1 g/cm^3 and 78 g/mol , respectively. Thus, its molar concentration is 14.1 M . The total number of molecules of the pure DMSO in the probed volume is found to be $14.1 \text{ M} \times 1.5 \text{ } \mu\text{m}^3 = 2.1 \times 10^{-14} \text{ mol}$. As the density of the DMSO solution with a Mf of $5.5 \times 10^{-8}\%$ is between 1 g/cm^3 and 1.1 g/cm^3 , which is approximately identical to that of pure DMSO, the ratio of the number of molecules of the DMSO solution to that of the pure DMSO in the probed volume is approximately equal to their Mf ratio. The total number of molecules of the DMSO solution in the probed volume is $2.1 \times 10^{-14} \times 5.5 \times 10^{-8}\% / 100\% = 1.2 \times 10^{-23} \text{ mol}$. Therefore, the Mf ratio that approximately equals the ratio of the numbers of molecules under enhanced and unenhanced conditions is used to calculate the SERS enhancement factor of DMSO.

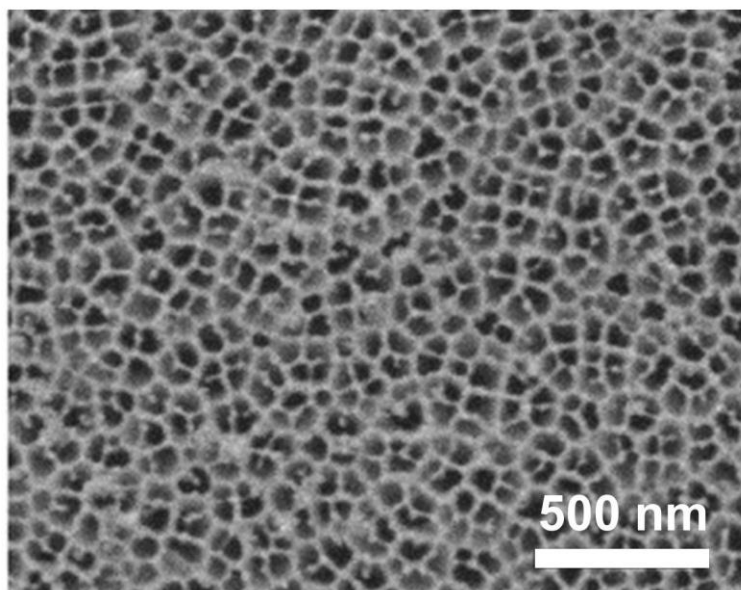
Comparison with different types of SERS substrates

We compare different types of SERS substrates, namely, Au, Ag, MoS_2 , Al_xO_3 , and graphene in terms of photothermal heat generation, reproducibility, biocompatibility, and enhancement factor, as shown in Supplementary Table 1. For the traditional metal substrates (Au and Ag), they provide high enhancement factors that depend on hot spots, but suffer from large photothermal heat generation, seriously limiting their reproducibility. For the semiconductor nanostructures (MoS_2 and Al_xO_3), their enhancement factors are on the order of 10^4 - 10^5 . Due to the inherent photocatalytic activity and the toxicity of the substrate materials to biomolecules, the semiconductor nanostructures suffer from poor biocompatibility. On the other hand, as a carbon allotrope, graphene exhibits excellent biocompatibility. Moreover, due to the fluorescence-quenching effect of graphene, it has been used in conjunction with other metal nanostructures for SERS measurements, which is known as graphene-enhanced Raman scattering (GERS). However, the enhancement factor of GERS is normally moderate ($\sim 10^3$) compared with the pure metal substrates. Among the previous substrates, the PCNA exhibits a high enhancement factor ($\sim 10^6$) with low heat generation, high reproducibility, and high biocompatibility.

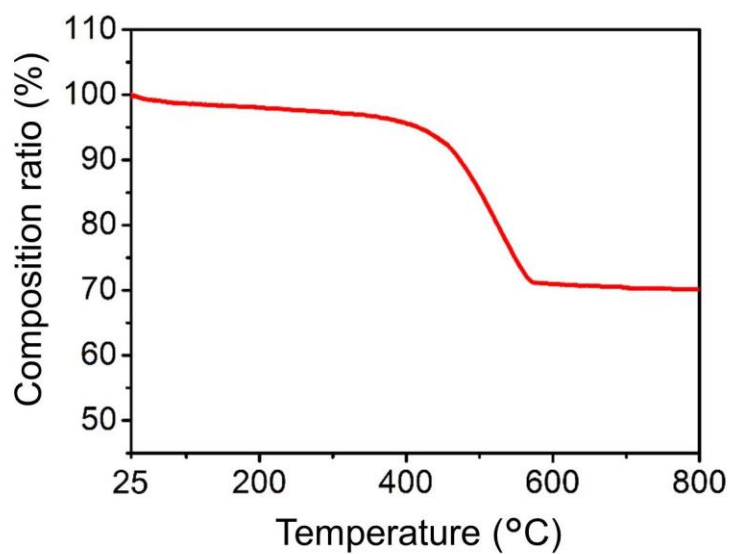
References

1. Kim, T. W. *et al.* A synthetic route to ordered mesoporous carbon materials with graphitic pore walls. *Angew. Chem. Int. Ed.* **42**, 4375-4379 (2003).

2. Hildebrandt, P. *et al.* Surface-enhanced resonance Raman spectroscopy of Rhodamine 6G adsorbed on colloidal silver. *J. Phys. Chem.* **88**, 5935-5944 (1984).
3. Jung, Y. M. *et al.* Two-dimensional infrared, two-dimensional Raman, and two-dimensional infrared and Raman heterospectral correlation studies of secondary structure of β -lactoglobulin in buffer solutions. *J. Phys. Chem. B* **104**, 7812-7817 (2000).
4. Koenig, J. L. *et al.* Raman scattering of Chymotrypsinogen A, Ribonuclease, and Ovalbumin in the aqueous solution and solid state. *Biochemistry* **11**, 2505-2520 (1972).
5. Mathlouthi, M. *et al.* Laser-Raman spectra of D-glucose and sucrose in aqueous solution. *Carbohydr. Res.* **81**, 203-212 (1980).
6. Selvarajan, A. Raman spectrum of dimethyl sulfoxide (DMSO) and the influence of solvents. *Proc. Indian Acad. Sci.* **64**, 44-50 (1966).
7. Gorobets, M. I. *et al.* Raman study of solvation in solutions of lithium salts in dimethyl sulfoxide, propylene carbonate and dimethyl carbonate. *J. Mol. Liq.* **205**, 98-109 (2015).
8. Shikata, T. *et al.* Dimeric molecular association of dimethyl sulfoxide in solutions of nonpolar liquids. *J. Phys. Chem. A* **116**, 990-999 (2012).
9. McMeekin, T. L. *et al.* Partial specific volume of the protein and water in beta - lactoglobulin crystals. *J. Polym. Sci.*, **12**, 309-315 (1954).
10. Camden J. P. *et al.* Probing the structure of single-molecule surface-enhanced Raman scattering hot spots. *J. Am. Chem. Soc.* **130**, 12616-12617 (2008).
11. Dasary, S. S. R. *et al.* Gold nanoparticle based label-free SERS probe for ultrasensitive and selective detection of trinitrotoluene. *J. Am. Chem. Soc.* **131**, 13806-13812 (2009).
12. Kang, L. *et al.* Recent progress in the applications of graphene in surface-enhanced Raman scattering and plasmon-induced catalytic reactions. *J. Mater. Chem. C* **3**, 9024-9037 (2015).
13. Huang, S. *et al.* Molecular selectivity of graphene-enhanced Raman scattering. *Nano Lett.* **155**, 2892-2901 (2015).
14. Feng, S. M. *et al.* Ultrasensitive molecular sensor using n-doped graphene through enhanced Raman scattering. *Sci. Adv.* **2**, e1600322 (2016).
15. Zheng, Z. H. *et al.* Semiconductor SERS enhancement enabled by oxygen incorporation. *Nat. Commun.* **8**, 1993 (2017).
16. Cong, S. *et al.* Electrochromic semiconductors as colorimetric SERS substrates with high reproducibility and renewability. *Nat. Commun.* **10**, 678 (2019).



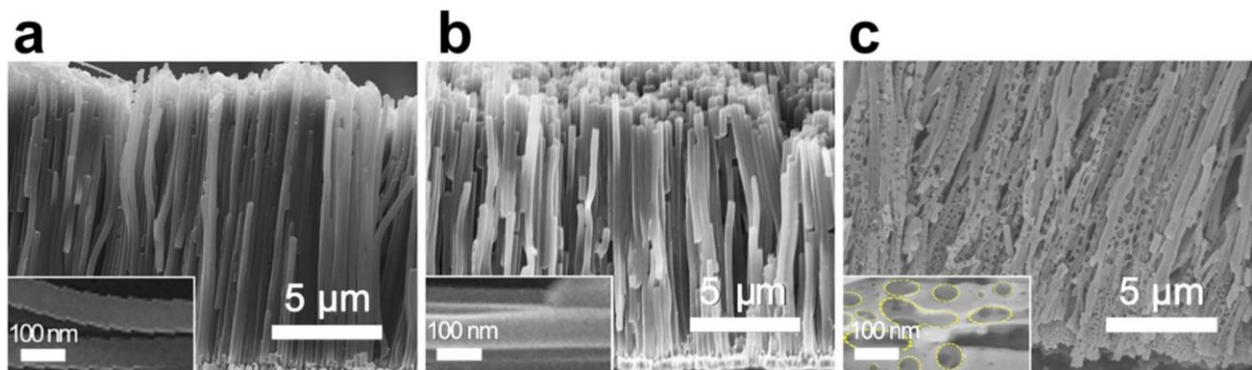
Supplementary Fig. 1 | SEM image of the AAO template with a porosity of 50-60%. The pores in the AAO template have a diameter of between about 100 and 150 nm.



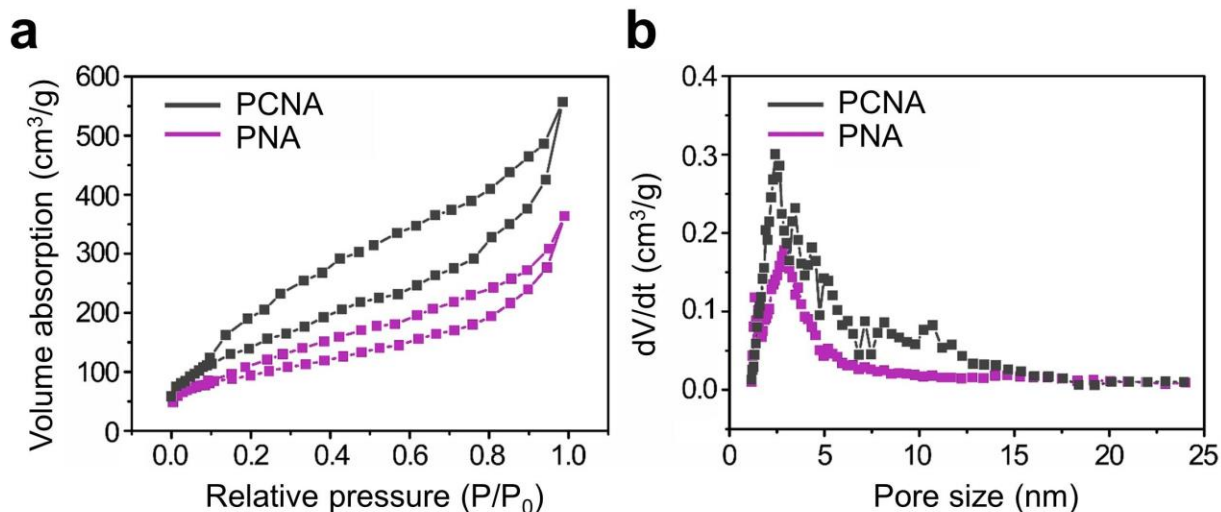
Supplementary Fig. 2 | Thermogravimetric analysis of the PNA. The measurement shows that the PNA began to lose its PPy ratio and became carbonized at a temperature of 500 °C. In addition, the sample has no significant weight loss above 600 °C. In order to carbonize the PNA, we chose 800 °C.



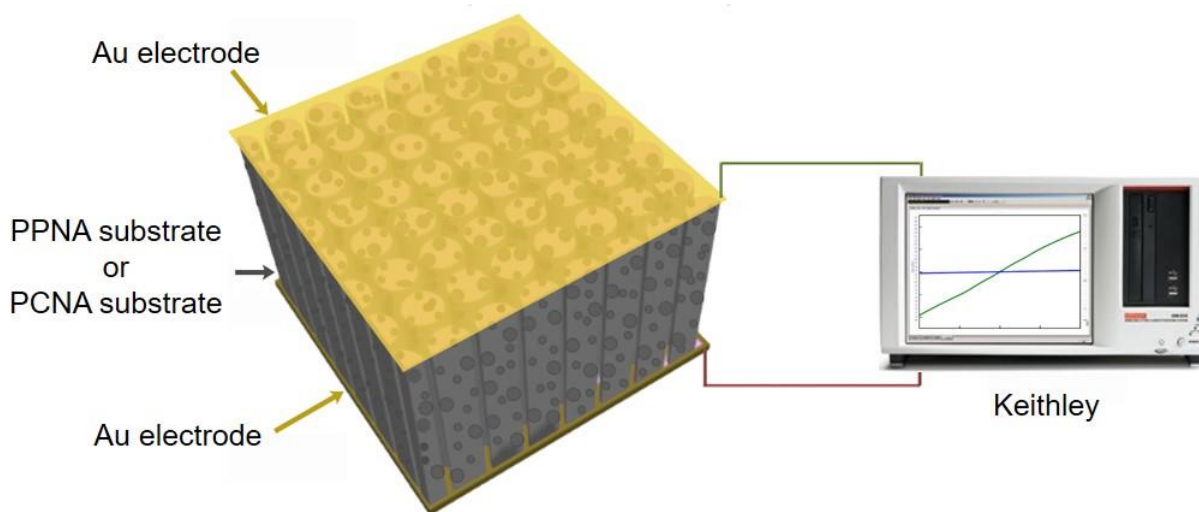
Supplementary Fig. 3 | Picture of the PCNA substrate on the PTFE plate. It is evident from the picture that the PCNA substrate has a diameter of about 12 mm.



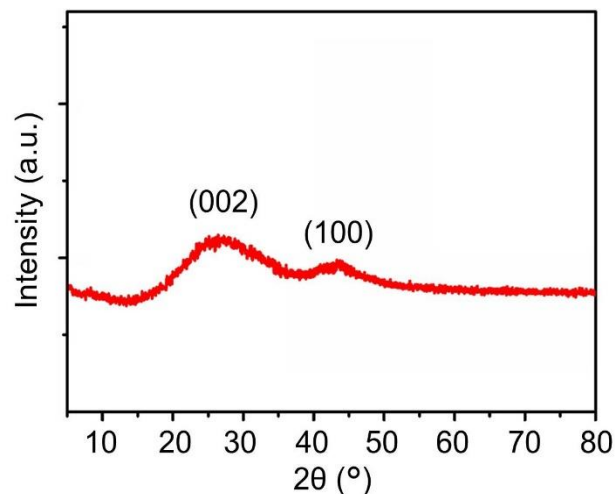
Supplementary Fig. 4 | a, PNA substrate. b, CNA substrate. c, PCNA substrate. The insets show enlarged images of the PNA, CNA, and PCNA substrates. In the inset of (c), the yellow dotted circles indicate micropores on the PCNA.



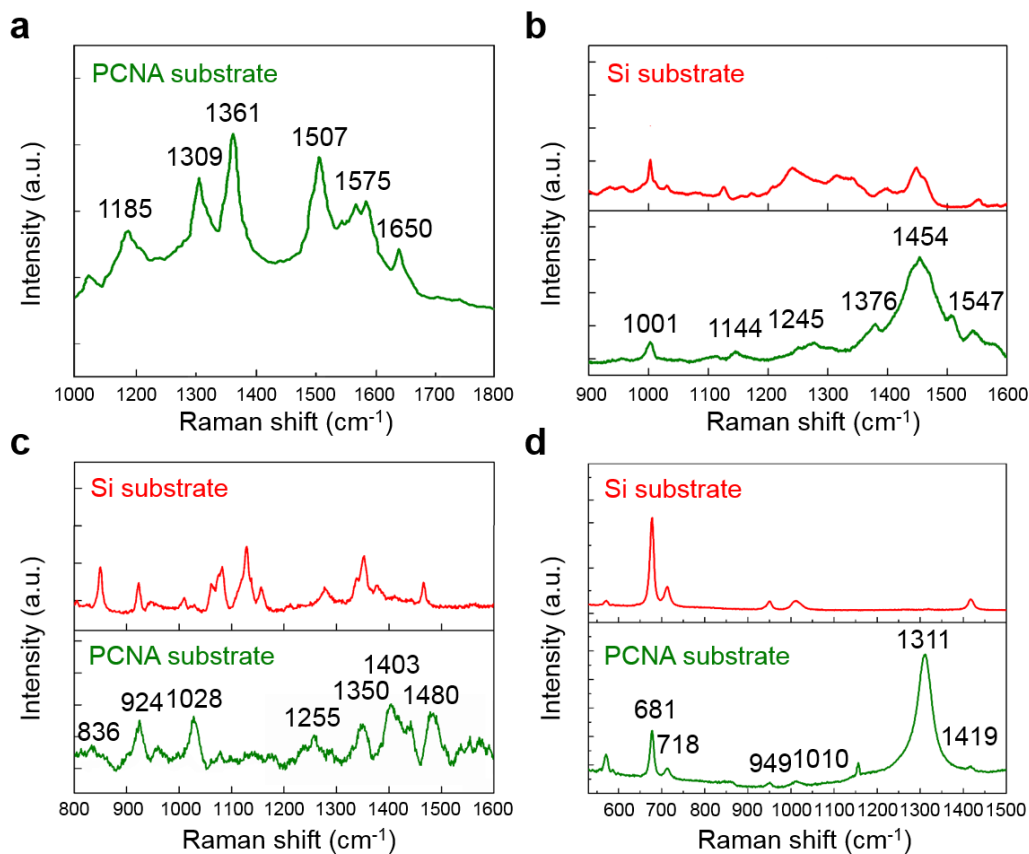
Supplementary Fig. 5 | Nitrogen adsorption-desorption isotherm measurements of the PNA and PCNA substrates. **a**, N₂ adsorption-desorption isotherms of the PNA and PCNA substrates. The hysteresis loop of the PCNA substrate is larger than that of the PNA substrate, which indicates the number of pores increased in the substrate. **b**, Pore size distributions of the PNA and PCNA substrates.



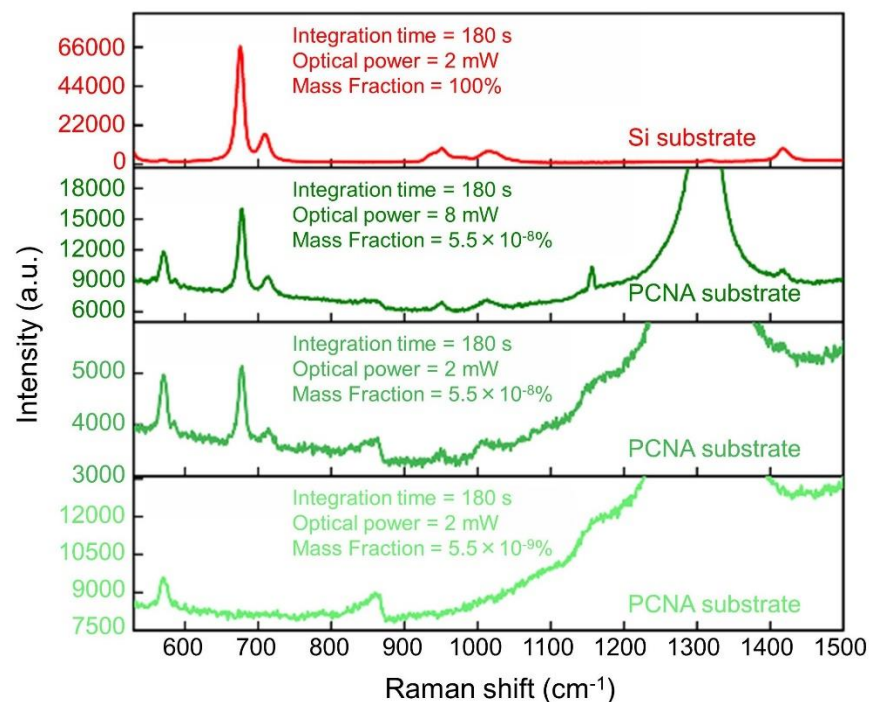
Supplementary Fig. 6 | Schematic of the *I-V* measurement setup of the PPNA and PCNA substrates. The PCNA substrate with an effective area of about $0.5 \times 0.5 \text{ mm}^2$ was put on an Au sheet electrode and covered with another Au sheet electrode on the top of the PCNA substrate to ensure that the two Au sheet electrodes were separated. All the substrates in our experiments were developed in a top-contact device configuration. The *I-V* characteristics of the substrates were recorded with a Keithley 4200 at room temperature in air.



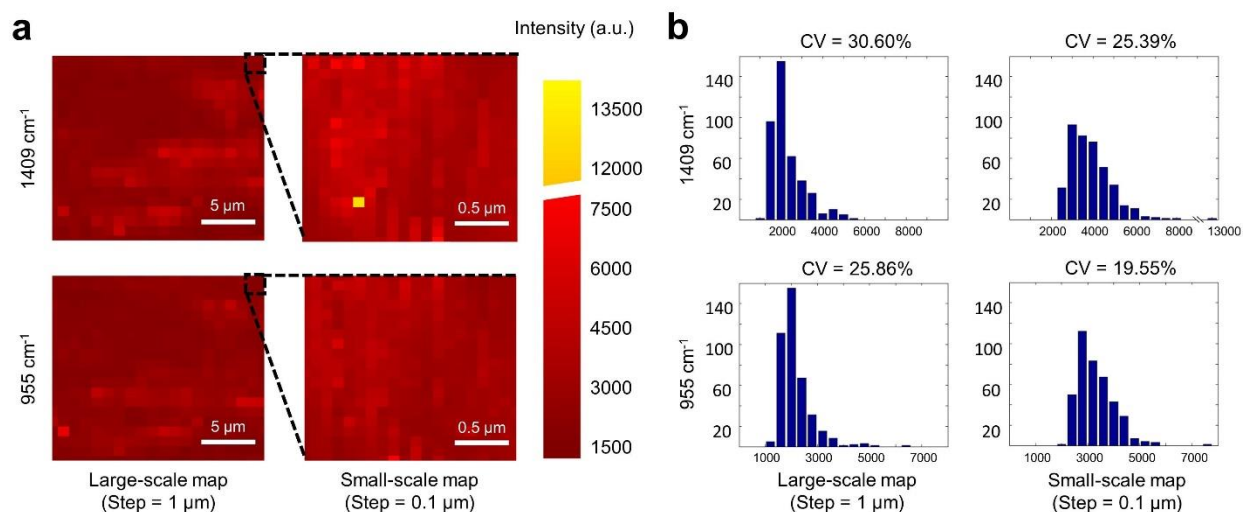
Supplementary Fig. 7 | XRD spectrum of the PCNA substrate. There are two diffraction peaks at 26° and 44° in the XRD spectrum, which correspond to the characteristic peaks of graphite. The results indicate the PPNA partially transformed to graphitized carbon after the carbonization process.



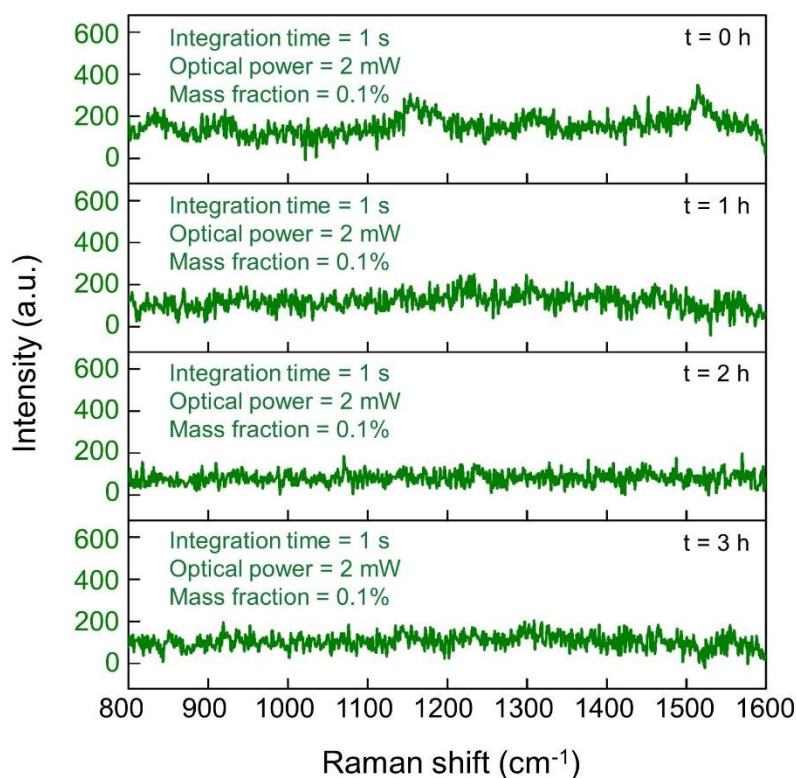
Supplementary Fig. 8 | Raman peak assignments of R6G, β-lactoglobulin, glucose, and DMSO. a, R6G. b, β-lactoglobulin. c, glucose. d, DMSO.



Supplementary Fig. 9 | Raman spectra of the DMSO on the silicon and PCNA substrates. Measured Raman spectra of the DMSO solutions with different mass fractions on the silicon and PCNA substrates. With the enhancement of the PCNA substrate, all the Raman peaks of the DMSO solutions were identifiable even at the very low mass fraction of $5.5 \times 10^{-8}\%$.



Supplementary Fig. 10 | SERS mapping of β -lactoglobulin on the commercial metal substrate. **a**, SERS maps on the metal substrate, showing high surface inhomogeneity in enhancement factor at two characteristic Raman shifts of β -lactoglobulin on both large and small scales with a step size of 1 μm and 0.1 μm , respectively. **b**, Histograms of the enhancement factors on the large and small scales.



Supplementary Fig. 11 | Time-to-time fluctuations of the commercial metal substrate in Raman spectrum. Except for the small Raman peaks at $t = 0$ h, there are almost no peaks in the Raman spectra at $t = 1$ -3 h, showing poor reproducibility.

Supplementary Table 1 | Comparison of different types of SERS substrates.

Material	Heat generation	Reproducibility	Biocompatibility	Enhancement factor	Ref.
Metal (Ag)	High	Very poor	Poor	10^9 at hot spots 10^5 on average	10
Metal (Au)	High	Very poor	Poor	10^9 at hot spots 10^5 on average	11
Graphene	Low	Poor	High	Less than 10^3	12-14
Semiconductor (MoS_2)	Low	Poor	Poor	10^5	15
Semiconductor (Al_xWO_3)	Low	High	Poor	10^4	16
PCNA	Low	Very high	High	10^6	This work

Supplementary Table 2 | Assignment of major peaks in the Raman spectra of measured samples.

Sample	Wavenumber (cm ⁻¹)	Assignment
R6G	1185	C–H bending
	1309	C–C stretching
	1361	C–C stretching
	1507	C–C stretching
	1575	C–C stretching
	1650	C–C stretching
β-lactoglobulin	1001	Phenylalanine
	1144	C–N stretching
	1245	Amide III (β-sheet)
	1376	C–H deformation, Tryptophan
	1454	CH ₃ (asymmetric), CH ₂ , CH bending
	1547	Tryptophan
glucose	836	C–C stretching
	924	C–H bending
	1028	C–O stretching
	1255	CH ₂ twisting
	1350	CH ₂ wagging
	1403	CH ₂ bending
	1480	CH ₂ bending
DMSO	681	C–S stretching
	718	C–S stretching
	949	C–H bending
	1010	S=O stretching
	1311	C–H deformation
	1419	CH ₃ deformation

Supplementary Table 3 | Estimated numbers of molecules of the measured samples in the probed volume.

Sample	Probed volume (μm^3)	Density (g/cm^3)	Mass fraction (%)	Molar concentration (M)	Number of molecules (mol)
β -lactoglobulin powder	1.5	1.25	100	6.8×10^{-2}	1.0×10^{-16}
β -lactoglobulin solution	1.5	1-1.25	0.4	2.7×10^{-4}	4.0×10^{-19}
glucose powder	1.5	1.54	100	8.7	1.3×10^{-14}
glucose solution	1.5	1-1.54	0.1	8.7×10^{-3}	1.3×10^{-17}
DMSO	1.5	1.1	100	14.1	2.1×10^{-14}
DMSO solution	1.5	1-1.1	5.5×10^{-8}	7.8×10^{-9}	1.2×10^{-23}